



Self-assembled materials with an ordered hydrophilic bilayer for high performance inverted Perovskite solar cells

Received: 2 August 2024

Accepted: 16 December 2024

Published online: 02 January 2025

Check for updates

Geping Qu^{1,2,9}, Letian Zhang^{1,9}, Ying Qiao^{1,9}, Shaokuan Gong^{3,9}, Yuanjia Ding^{1,9}, Yuli Tao⁴, Siyuan Cai¹, Xiao-Yong Chang¹, Qian Chen¹, Pengfei Xie¹, Junyuan Feng¹, Changqin Gao¹, Guopeng Li¹, Hui Xiao⁵, Fei Wang⁶, Hanlin Hu⁶, Jie Yang⁷, Shi Chen⁷, Alex K.-Y. Jen^{1,8} ✉, Xihan Chen³ ✉ & Zong-Xiang Xu^{1,8} ✉

While self-assembled material based inverted perovskite solar cells have surpassed power conversion efficiencies of 26%, enhancing their performance in large-area configurations remains a significant challenge. In this work, we report a self-assembled material based hole-selective layer 4-(7H-dibenzo[c,g]carbazol-7-yl)phenyl)phosphonic acid, with a π -expanded conjugation. The enhanced intermolecular π - π interactions facilitate the self-assembly of 4-(7H-dibenzo[c,g]carbazol-7-yl)phenyl)phosphonic acid molecules to form an ordered bilayer with a hydrophilic surface, which passivates the buried perovskite interface defect and enables high-quality and large-area perovskite preparation, while simultaneously enhancing interfacial charge extraction and transport. The certified efficiency of 4-(7H-dibenzo[c,g]carbazol-7-yl)phenyl)phosphonic acid based small-area (0.0715 cm²) device is 26.39% with high stability. Furthermore, a certified efficiency of 25.21% is achieved for a 99.12 mm² large area device.

Recently, self-assembled materials (SAMs) have garnered significant interest for their utility as hole-selective layers (HSLs) within inverted perovskite solar cells (IPSCs) and in the construction of perovskite-based tandem solar cells, as documented in references^{1–4}. They offer several advantages, such as adjustable energy levels, low synthetic cost, minimal parasitic absorption, and the ability to passivate the defects of upper layer perovskites and transparent conductive oxide (TCO) substrates^{5,6}.

Although SAM-based IPSCs have demonstrated impressive power conversion efficiencies (PCEs) over 26%^{7,8}, further improving the efficiency or fabricating high-performance large-area IPSCs remains quite challenging due to the frequently encountered SAM assembly defects and wettability issue due to incompatibility between the non-polar head groups with polar perovskite precursor solutions. Various strategies have been developed to address these issues, such as co-assembly of different head groups SAMs^{7,9,10}, incorporating insulating

¹Department of Chemistry, Southern University of Science and Technology, Shenzhen, Guangdong, China. ²Department of Materials Science and Engineering, City University of Hong Kong, Kowloon, Hong Kong, China. ³Department of Mechanical and Energy Engineering, SUSTech Energy Institute for Carbon Neutrality, Southern University of Science and Technology, Shenzhen, Guangdong, China. ⁴University of Science and Technology of China, Hefei, China. ⁵Key Laboratory of Bioelectrochemistry & Environmental Analysis of Gansu Province, College of Chemistry & Chemical Engineering, Northwest Normal University, Lanzhou, China. ⁶Hoffmann Institute of Advanced Materials, Shenzhen Polytechnic University, Shenzhen, Guangdong, China. ⁷Henan Key Laboratory of Quantum Materials and Quantum Energy, School of Quantum Information Future Technology, Henan University, Zhengzhou, China. ⁸Guangdong-Hong Kong-Macao Joint Laboratory for Photonic-Thermal-Electrical Energy Materials and Devices, Southern University of Science and Technology, Shenzhen, Guangdong, China. ⁹These authors contributed equally: Geping Qu, Letian Zhang, Ying Qiao, Shaokuan Gong, Yuanjia Ding. ✉ e-mail: alexjen@cityu.edu.hk; chenxh@sustech.edu.cn; xu.zx@sustech.edu.cn

materials like Al_2O_3 , and combining SAMs with NiO_x ^{11,12}. However, these strategies increase the complexity of devices preparation and materials while reducing cost-saving and efficiency-boosting benefits of SAMs. The fabrication of SAM films typically involves the application of a low-concentration solution followed by rinsing to produce single-layer films for high-efficiency devices. Notably, increasing the concentration of SAM solution to create thicker films may reduce film defects, however, this approach has not been widely adopted due to its negative impact on charge transport in thicker films. An amphiphilic SAM, designated as MPA-CPA, featuring a versatile cyanovinyl phosphonic acid (PA) anchoring group, has been demonstrated to effectively fabricate multilayer stacks for large-area IPSCs. Impressively, these stacks achieve a PCE exceeding 23%, obviating the need for rinsing when used at higher concentrations¹³. However, its performance still falls short compared to traditional hole transport layers made from metal oxides¹² or polymers¹⁴. Therefore, finding rational designs of SAMs that do not introduce negative effects while still achieving high performance along with large area remains a significant challenge in the field of perovskite photovoltaics.

To efficiently design SAMs, a three-component model consisting of an anchoring, linker, and functional head group can be utilized based on their shared characteristics. Notably, the synergistic modulation of the assembly of SAMs utilizing these components necessitates careful consideration during the molecular design process^{15–20}. Since the first demonstration of using a carbazole-containing SAM with a PA anchoring group to achieve PCE of 17.8% in IPSC²¹, numerous modifications of carbazole head groups have been investigated to optimize SAMs properties and enhance the performance of IPSCs^{9,22–25}. Notably, the helical π -expansion of carbazole, such as (4-(7*H*-dibenzo[*c,g*]carbazol-7-yl)butyl)phosphonic acid (Bz-4PACz), has shown potential in increasing both the SAM dipole moment and π - π interactions. This led to the formation of a densely packed and ordered monolayer with a suitable energy level to align with the perovskite absorber, effectively enhancing hole extraction. This approach resulted in an increased PCE to 24%²⁴ and large area-all perovskite tandem solar cells containing PCE up to 27.0%³.

By further utilizing the benefits of conjugated linkers in SAM design^{17,19}, we developed a functionalized SAM denoted 4-(7*H*-dibenzo[*c,g*]carbazol-7-yl)phenyl)phosphonic acid (Bz-PhpPACz) derived from (4-(9*H*-carbazol-9-yl)phenyl) phosphonic acid (PhpPACz) (Fig. 1a)¹⁹, and utilized as an HSL for IPSCs. Bz-PhpPACz contained a π -expanded carbazole, phenylene, and PA as head, linker, and anchoring groups, respectively. Molecular structure of Bz-PhpPACz was recently published and shown to form a highly crystalline self-assembled multilayer, resulting in small-area IPSCs with a PCE of 26.07%²⁶. In this study, we have further demonstrated that the enlarged conjugation of SAM Bz-PhpPACz enhances intermolecular π - π interactions and facilitates the self-assembly of molecules into an ordered bilayer structure with a hydrophilic surface by selecting proper solvents and perovskite composition as well as modifying the SAM solution concentration. The results show that the ordered hydrophilic bilayer structure of Bz-PhpPACz leads to certified PCEs of 26.39% and 25.21% for small-area (0.0715 cm²) and large-area (99.12 mm²) IPSCs, respectively, along with excellent stability.

Results

Development and characterization of hole-selective layer

The molecular design and chemical structure of Bz-PhpPACz are depicted in Fig. 1a, while the synthesis and characterization data can be found in the supplementary materials section with verified molecular structure, and *p*-type semiconductor characteristics with high thermal stability, which is advantageous for its application as an HSL in IPSCs (Supplementary Figs. 1–13).

Molecular interactions and packing modes are crucial factors in the self-assembly process of SAMs. Single crystals of SAMs including

Bz-4PACz, PhpPACz and Bz-PhpPACz were successfully grown and utilized to elucidate these forces, providing valuable insights (Supplementary Data 1–3 and Supplementary Table 1). Figure 1b shows the Bz-PhpPACz crystal structure, with a view along the *b* axis showing the layered structure with two phosphate groups up (blue) and the other two phosphate groups down (red) in each repeating unit. The side view of the repeating units shows the intermolecular π - π interactions in each layer, which was consistent with the view along the normal direction of two parallel staggered phenyl rings (yellow glow), with a close face-to-face distance of 3.409 Å. By contrast, the face-to-face π - π interactions were absent in the single crystal structures of Bz-4PACz and PhpPACz (Supplementary Figs. 14, 15), which demonstrated the strongest molecular packing of Bz-PhpPACz among three molecules. These findings were in line with the theoretical calculations of interaction forces for SAMs, as shown in Supplementary Fig. 16, indicating a closest intermolecular distance of 3.66 Å for Bz-PhpPACz.

This strong molecular interaction of Bz-PhpPACz was further confirmed by theoretical simulations. *Ab initio* molecular dynamics (AIMD) simulations were initially utilized to examine the arrangement of single and multiple Bz-PhpPACz molecules on fluorine doped tin oxide (FTO) surface (Supplementary Figs. 17, 18). As shown in Fig. 1c and Supplementary Fig. 18, after 10 ps of AIMD simulations, the outcomes revealed that multiple Bz-PhpPACz molecules were aligned parallel to one another on the FTO surface with an interatomic distance of 2.96 Å, which was possibly the driving force for the self-assembling process. These computational findings were consistent with the single crystal analysis.

The enhanced π - π interactions resulting from the π -expansion and the strong interactions between the PA group and metal oxide in Bz-PhpPACz were possibly beneficial for creating a densely packed and the ordered self-assembly HSL for IPSCs. Inspired by the phospholipid bilayer structure²⁷, we proposed that under optimal conditions an ordered hydrophilic bilayer structure can form during IPSC fabrication, consisting of a chemically anchored SAM monolayer plus a non-adsorbed, ordered second layer with the presence of PA at the buried interface between perovskite (Fig. 1d).

The ordered bilayer structure has shown to be crucial for high-performance IPSCs. Static density functional theory (DFT) calculations revealed that the interactions between the expanded carbazole head of Bz-PhpPACz molecule and perovskite was almost negligible (−0.01 eV, Fig. 1e), while the interaction between the PA end and perovskite was −0.80 eV (Supplementary Fig. 19). However, when bilayer Bz-PhpPACz molecules were adsorbed on perovskite, the interaction significantly strengthened, reaching −5.41 eV (Fig. 1e). These results suggested that the bilayer Bz-PhpPACz molecules had a higher affinity for adsorption onto the perovskite surface, which could be advantageous for perovskite defect passivation as well as charge extraction. Secondly, as shown by the smaller water droplet contact angle (Fig. 1d), the Bz-PhpPACz bilayer structure exhibited more hydrophilic properties compared to the monolayer, and displayed better wetting characteristics with the perovskite precursor solution (Supplementary Figs. 20, 21 and movies 1–7). This could help form large-area perovskite thin films. The strong interactions with perovskites and the higher hydrophilicity of the Bz-PhpPACz bilayer resulted in a certified PCE of 26.39% for small-area IPSC and a PCE of 25.44% for 1 cm² large-area devices (Fig. 1f).

Examination of bilayer structure for hole-selective layer

To confirm our previous findings, SAM films were prepared using a spin-coating technique and the concentration was optimized with and without rinsing (Fig. 2a). The PCE of Bz-PhpPACz without rinsing was observed to increase initially then decrease with increasing concentration, with 2.8 mM identified as the optimal concentration. The sample was labeled as Bz-PhpPACz (2.8 mM) (Fig. 2b and Supplementary Fig. 22). By contrast, the performance of the devices using

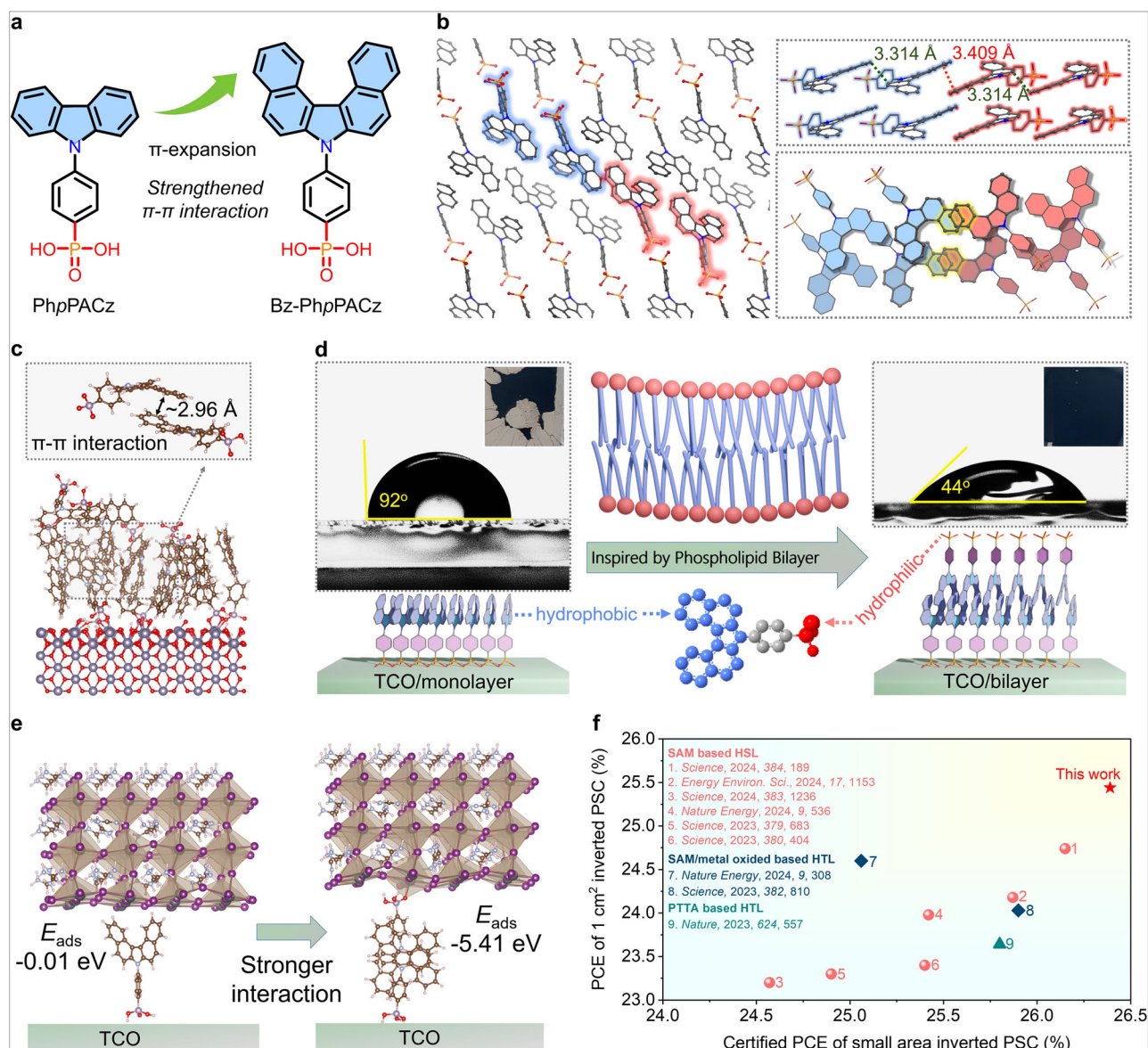


Fig. 1 | Molecular interaction of SAM molecules and proposed bilayer structure.

a Molecular design strategy and structure of Bz-PhpPACz. **b** Packing patterns in the single crystal structure of Bz-PhpPACz with strong interlayer π - π stacking. **c** Final configurations of multiple bilayers of Bz-PhpPACz molecules stacking onto the FTO surface after a 10 ps of AIMD simulation. **d** Proposed bilayer structure of Bz-

PhpPACz mimicking from phospholipid bilayer and its corresponding enhanced hydrophilicity with water drop contact angles of 92° and 44° for single layer and bilayer, respectively. **e** Configurations of the Bz-PhpPACz molecules that adsorbed on the FAPbI₃ perovskite surface through the carbazole end and the PA anchoring group, respectively. **f** Reported PCE of IPSCs with small and 1 cm² device areas.

reported Bz-4PACz SAM without rinsing decreased with increasing concentration (Supplementary Fig. 23). In the preparation of monolayer SAM films, Bz-PhpPACz samples were thoroughly rinsed with isopropanol (Fig. 2a and Supplementary Fig. 24). Interestingly, the efficiency of these rinsed Bz-PhpPACz samples was consistently lower than that of the Bz-PhpPACz sample without rinsing at all concentrations. It is worth noting that the rinsing sample with a concentration of 2.8 mM, which demonstrated the highest PCE, was labeled as Bz-PhpPACz (r). For Bz-4PACz, the rinsing sample demonstrated the best performance, which was possibly related to the formation of different layer structures of SAMs.

To validate the ordered bilayer SAM structure, X-ray photoelectron spectroscopy (XPS) quantification was performed. With the increase in the preparation concentration of Bz-PhpPACz, there was a significant increase in the N/Sn and P/Sn ratios (Supplementary Figs. 25, 26 and Supplementary Table 2). For Bz-PhpPACz washed with perovskite precursor solution, the maximum values were achieved at a

concentration of 2.8 mM. These results demonstrated an increase in the number of SAM molecules, even after washing with a perovskite precursor solvent (Fig. 2c, Supplementary Figs. 27, 28 and Supplementary Table 2). By contrast, for Bz-4PACz, the N/Sn and P/Sn ratios slowly increased with increasing concentrations, indicating the washing process removed significantly more Bz-4PACz molecules, maintaining an almost constant ratio at 2.1–2.8 mM (Supplementary Figs. 29, 30). The higher N/Sn and P/Sn ratios of Bz-PhpPACz compared to Bz-4PACz also revealed the denser packing properties¹⁹.

X-ray reflectivity (XRR) measurements were carried out and combined with theoretical calculations to determine the film thickness of SAM (Fig. 2d, Supplementary Figs. 31–33 and Supplementary Table 3)^{19,28–30}. The results showed that at a low concentration of 0.7 mM, the thickness of Bz-PhpPACz was 6.49 Å, which was consistent with the theoretically calculated value for a single molecule adsorbed on FTO (Fig. 2d). As the concentration increased, the thickness also increased and reached a maximum value of 13.46 Å at 2.8 mM, which

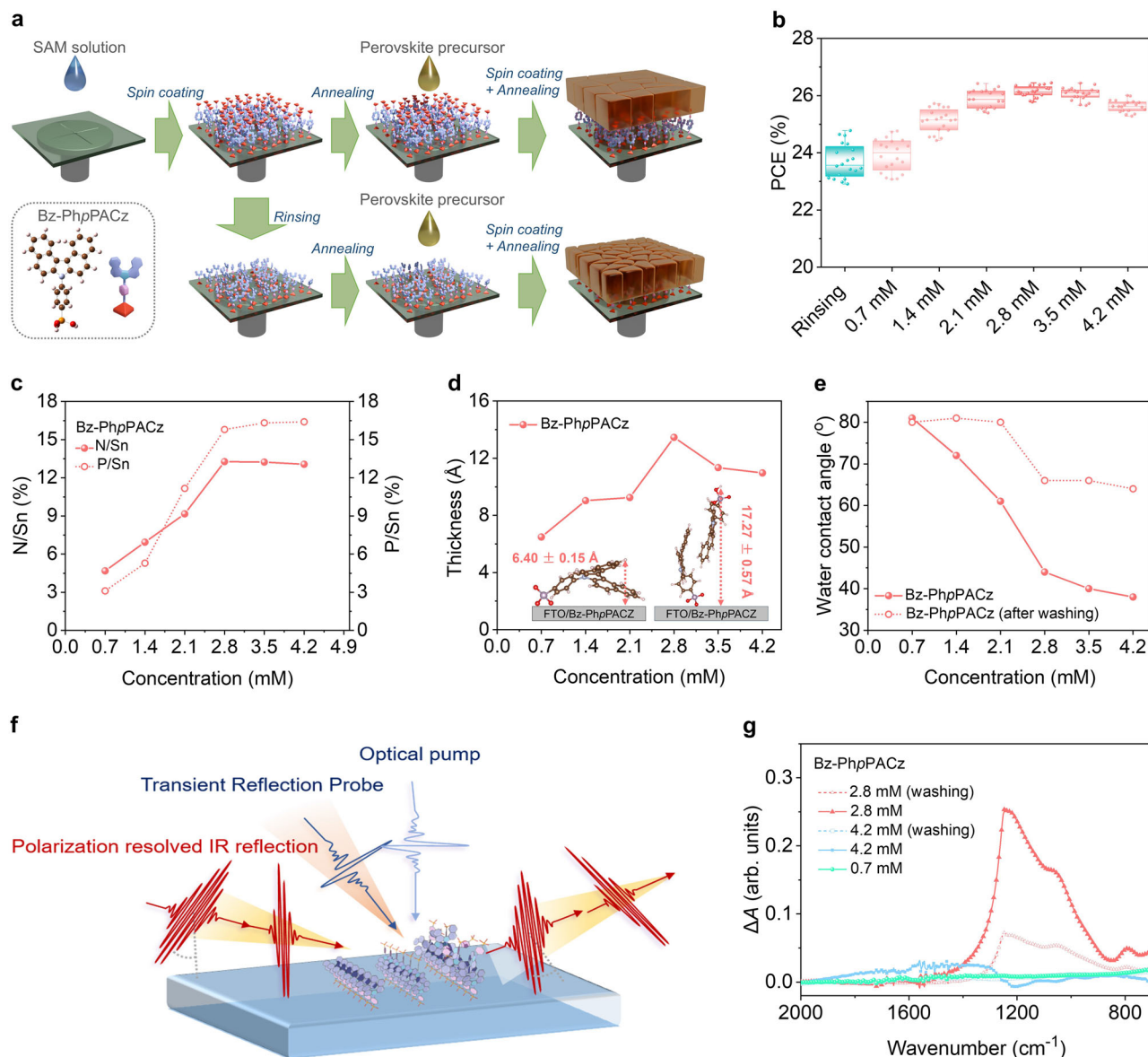


Fig. 2 | Thin film fabrication and characterizations. **a** Scheme of the fabrication process of SAM and perovskite thin films. **b** Statistics of PCEs for Bz-PhpPACz based IPSCs. The box plot denotes the median (center line), 75th (top edge of the box), and 25th (bottom edge of the box). **c** N/Sn and P/Sn ratios for Bz-PhpPACz/FTO derived from XPS measurements. **d** Bz-PhpPACz thin films thickness derived from

the RRR measurements (inset: theoretical calculated lengths for mono- and bi-molecule adsorbed on FTO). **e** Water contact angles of Bz-PhpPACz thin films fabricated with varied concentrations. **f** Scheme illustration and **(g)** Related spectra of polarization-resolved grazing incidence infrared reflection spectroscopy measurements.

was close to the theoretically calculated value for bimolecular packing on FTO and indicated the formation of a bilayer structure. By contrast, the thickness of Bz-4PACz remained constant at approximately 4 Å for varied concentrations (Supplementary Fig. 32).

Since the monolayer structure of Bz-PhpPACz showed more hydrophobic properties, the formation of bilayer structure could be verified through the exposure of PA group of Bz-PhpPACz related with higher hydrophilicity. Water contact angle measurements were conducted on films fabricated with different concentrations before and after washing with the perovskite precursor solvent by spin-coating (Supplementary Figs. 20, 34). As shown in Fig. 2e, the contact angle for Bz-PhpPACz decreased with increasing concentration before washing, approaching that of bisphosphonic acid SAM at 2.8 mM or higher (Supplementary Fig. 35). After washing, samples with concentrations between 0.7 and 2.1 mM retained a large contact angle of around 80°, indicating an exposed hydrophobic carbazole group. However, at

2.8 mM or higher, the contact angle significantly decreased to less than 70°, suggesting the exposure of PA groups with more hydrophilic character. By contrast, the contact angles decreased with increasing concentration for Bz-4PACz before washing then remained constantly around 70° after washing (Supplementary Figs. 36–38). These results were consistent with the XRR measurements and confirmed the formation of a bilayer structure for Bz-PhpPACz with an optimized concentration of 2.8 mM. The Angle-resolved XPS analysis also revealed that the Bz-PhpPACz (2.8 mM) SAM has a bilayer structure with non-coordinated phosphonic acid groups on the surface and anchored groups at the TCO interface, with a thickness of approximately 1.97 nm (Supplementary Figs. 39–42).

To investigate the molecular orientation of SAM molecules on FTO, we conducted polarization-resolved grazing incidence infrared reflection spectroscopy measurements (Fig. 2f). By examining the difference between *p* (perpendicular to the FTO plane) and *s* (parallel

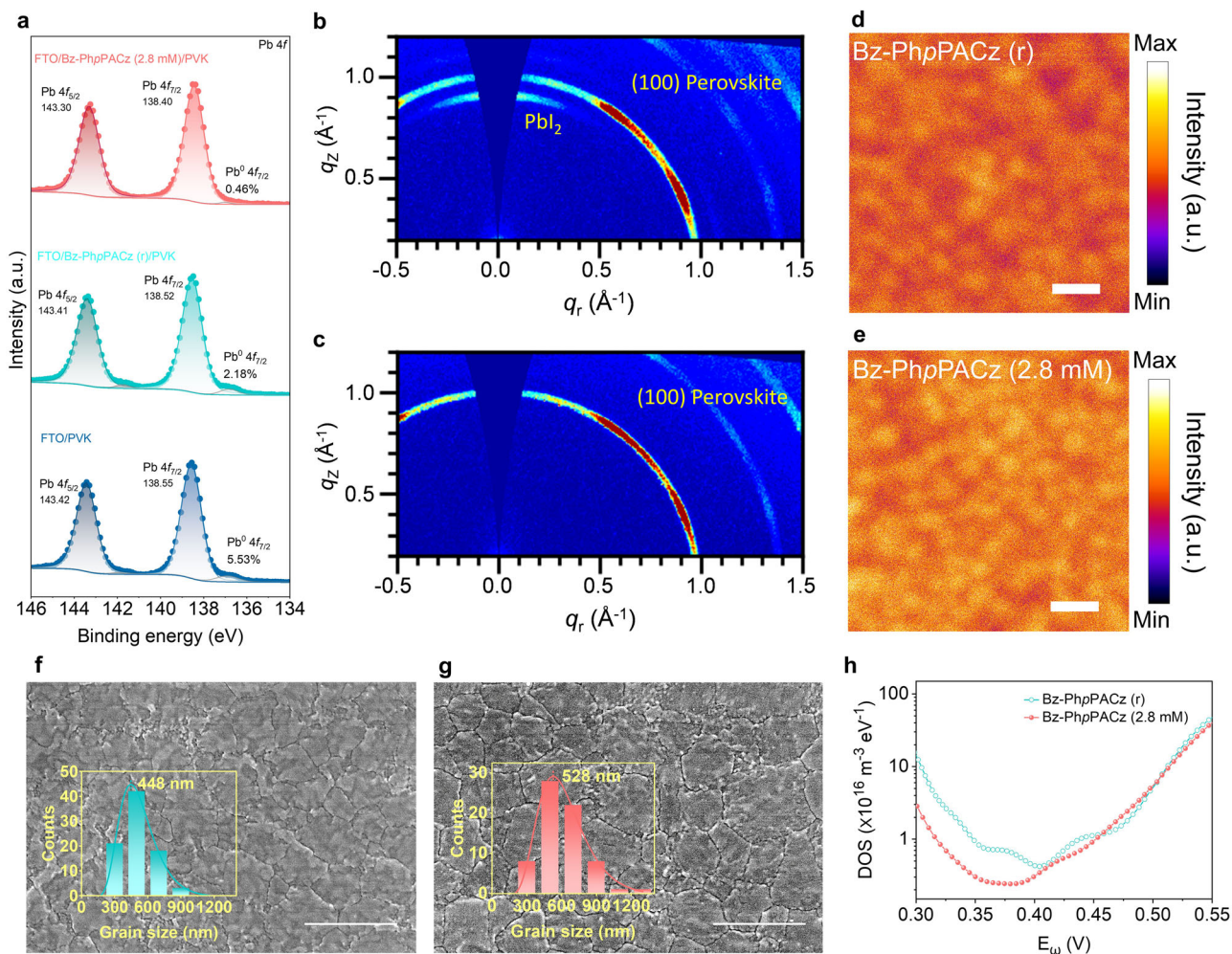


Fig. 3 | Thin film characterizations of perovskite deposited on Bz-PhpPACz.

a XPS Pb 4f spectra of the buried surface of the peeled off perovskite films deposited on different substrates. GIWAXS patterns of the perovskites deposited on **b** Bz-PhpPACz (r) and **c** Bz-PhpPACz (2.8 mM). PL mapping of the perovskites

deposited on **d** Bz-PhpPACz (r) and **e** Bz-PhpPACz (2.8 mM) (scale bar of 1 μm). SEM images and corresponding grain size statistics of the buried surface for the peeled off perovskite films deposited on **f** Bz-PhpPACz (r) and **g** Bz-PhpPACz (2.8 mM) (scale bar of 1 μm). **h** TDOS analysis of perovskites.

to the FTO plane) polarization, we could assess the molecular orientation on the substrate. This is because the component of the dipole moment in the normal direction will be enhanced. The data was analyzed using $\Delta R = \frac{R_S - R_P}{R_S}$ to describe the difference (R_S is the raw IR reflectance in S-polarization, R_P is the raw IR reflectance in P-polarization and the calculated ΔR is the difference reflectance between S- and P-polarization). To simplify this expression, we have used ΔR for the Kramers-Kronig transformation to obtain the absorption (ΔA) intensity as shown in Fig. 2g and Supplementary Fig. 43. Comparing the Bz-PhpPACz samples prepared under different conditions, it can be observed that the absorption strength of the 2.8 mM sample was significantly higher, indicating a better vertical orientation for PA group. Furthermore, a prominent absorption peak of the 2.8 mM sample was observed even after washing treatment, supporting the conclusion of forming a stable bilayer structure^{31–33}.

Examination of perovskite thin film

As shown in Fig. 1d, e, the bilayer SAM structure had a strong interaction with perovskite and the PA group stood vertically for perovskite formation, which was advantageous for perovskite defect passivation. XPS analysis revealed that PA groups effectively passivated the perovskite at the buried interface (Supplementary Fig. 44 and Fig. 3a). The binding energy of the perovskite Pb^{2+} peak on FTO and FTO/Bz-PhpPACz (r) is almost identical. However, compared to FTO/Bz-

PhpPACz (r), the perovskite binding energy on FTO/Bz-PhpPACz (2.8 mM) decreases by approximately 0.12 eV, suggesting stronger coordination between the perovskite and phosphonic acid in SAM as a Lewis base. Metallic Pb clusters (Pb^0) were successfully verified iodide deficiency and could act as recombination centers, resulting in lower PCEs of PSCs³⁴. The Pb^0 area at the buried interface for FTO, FTO/Bz-PhpPACz (r), and FTO/Bz-PhpPACz (2.8 mM) decreases from 5.53% and 2.18% to 0.46%, respectively, at the buried interface, which could be attributed to the passivation effect of the PA group. Furthermore, the SAM molecules were not observed in the bulk phase of perovskite (Supplementary Fig. 45).

The grazing-incidence wide-angle X-ray scattering (GIWAXS) measurements were conducted to evaluate the quality of perovskites. As shown in Fig. 3b, c and Supplementary Fig. 46, the results revealed that the bilayer Bz-PhpPACz effectively inhibited the formation of PbI_2 and enhanced the radial integration intensity of the perovskite (100) crystal plane. These findings were further verified by the grazing-incidence X-ray diffraction (GIXRD) analysis of the perovskite buried interface (Supplementary Fig. 47).

Photoluminescence (PL) mapping showed that perovskites deposited on Bz-PhpPACz (2.8 mM) exhibited better uniformity and stronger emission intensity compared to Bz-PhpPACz (r) and Bz-4PACz samples, indicating improved thin film quality (Fig. 3d, e and Supplementary Fig. 48). The results were consistent with those from the PL

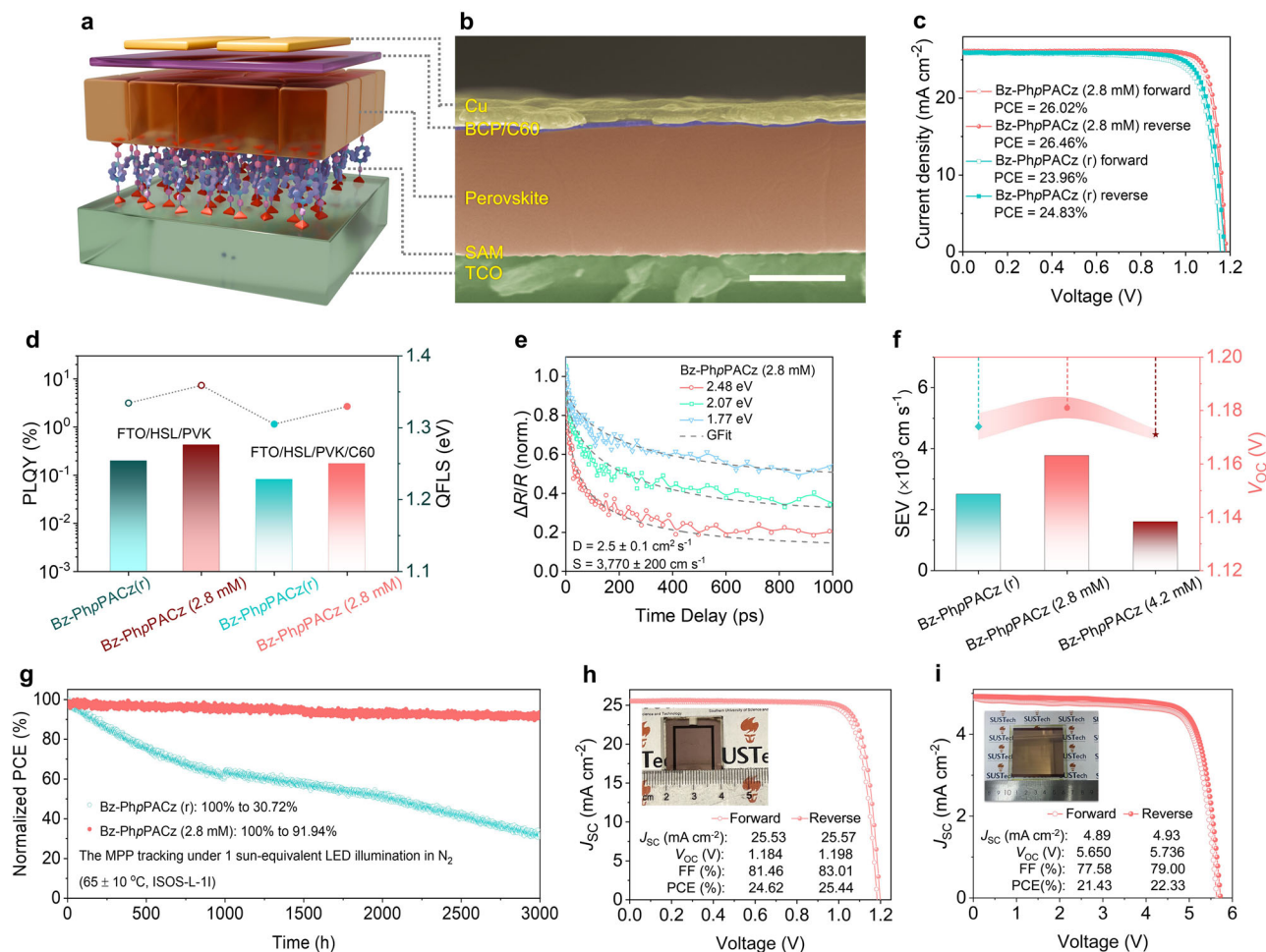


Fig. 4 | Configuration and photovoltaic performance of IPSCs. **a** Device structure of IPSC. **b** Cross-sectional SEM image of the Bz-PhpPACz (2.8 mM) based device (scale bar of 500 nm). **c** J - V curves of Bz-PhpPACz based devices. **d** PLQY and QFLS of perovskite films deposited on different substrates. **e** Surface carrier kinetics from extraction at 2.48, 2.07, and 1.77 eV probed by TR spectroscopy and fitted with a diffusion surface extraction model for perovskite deposited on Bz-PhpPACz

(2.8 mM). **f** Distribution of SEV values and V_{oc} values for perovskite films deposited on Bz-PhpPACz. **g** MPP tracking under N_2 and simulated 1 sun AM 1.5 G illumination for uncooled devices (reaching an operating temperature of $65 \pm 10^\circ C$). **h** J - V curves of large area IPSC (Inset: Photograph of large area IPSC). **i** J - V curves of mini module (Inset: Photograph of mini module).

and time-resolved PL (TRPL) measurements (Supplementary Fig. 49 and Supplementary Table 4).

As indicated by the scanning electron microscopy (SEM) images (Fig. 3f, g and Supplementary Fig. 50), the PA group passivation along with the better wettability collectively resulted in increased grain size on both the top and buried interfaces of perovskite grew on Bz-PhpPACz (2.8 mM), and this was possibly beneficial for reducing grain boundary defects. As shown in Fig. 3h, when the trap depth was below 0.4 eV, the trap density of states (TDOS) in Bz-PhpPACz (2.8 mM) devices are significantly decreased. Specifically, in the range of 0.3 eV to 0.4 eV, the TDOS of the Bz-PhpPACz (2.8 mM) device was 7 times lower than that of the Bz-PhpPACz (r) device. However, when the trap depth exceeds 0.40 eV, the difference in TDOS between the samples became negligible. This was because the TDOS in perovskites assigns deeper traps (>0.40 eV) to the surface defects and shallower traps (<0.40 eV) to the grain boundary defects. These results suggested that the bilayer structure of Bz-PhpPACz (2.8 mM) was particularly effective in reducing the perovskite defects and increasing the crystallinity.

Inverted perovskite solar cell performance

Device configuration of IPSC with an FTO/SAM/perovskite/C60/BCP/Cu structure is depicted in Fig. 4a, b and Supplementary Figs. 51, 52. The energy level of each material used in this work was obtained from

UV-vis absorption and ultraviolet photoelectron spectroscopy (UPS) measurements (Supplementary Figs. 53, 54) and depicted in Supplementary Table 5. The energy level diagrams of the IPSCs based on mono- and bi-layer HSL are shown in Supplementary Fig. 55, which demonstrated slightly increased ability for hole extraction and electron blocking for Bz-PhpPACz (2.8 mM).

The optimal J - V curves and corresponding photovoltaic parameters of IPSCs based on Bz-PhpPACz and Bz-4PACz are presented in Fig. 4c, Supplementary Fig. 56, and Supplementary Table 6. The reverse scan champion PCEs of Bz-PhpPACz (2.8 mM) and Bz-PhpPACz (r) devices were 26.46% and 24.83%, respectively, and these values were higher than that of Bz-4PACz. The certified PCE was 26.39%, according to the National PV Industry Measurement and Testing Center (NPVM) (Supplementary Fig. 57). Along with the integrated current obtained from external quantum efficiency (EQE) measurements (Supplementary Fig. 58), this increased PCE of Bz-PhpPACz (2.8 mM) could be attributed to enhanced current density (J_{sc}), open-circuit voltage (V_{oc}) and fill factor (FF), which was consistent with the average photovoltaic parameters of 20 devices. And it needed to be mentioned that Bz-PhpPACz exhibited high tolerance to concentration. Even fabricated with 4.2 mM, PCE of 25.63% was achieved, which is much higher than that of Bz-4PACz (PCE of 23.12%) (Supplementary Tables 7, 8).

The Bz-PhpPACz (2.8 mM)-based devices showed enhanced performance parameters like increased carrier mobility, reduced ideality factor (n_{ID}), and minimized resistance. (Supplementary Figs. 59, 60). Commonly observed factors contributing to FF values that fall short of the S-Q limit include trap-assisted non-radiative recombination and losses related to charge transport. The n_{ID} calculations reveal that the maximum FF (FF_{max}) achievable for Bz-PhpPACz (2.8 mM) and Bz-PhpPACz (r) is 87.6% and 84.46%, respectively (Supplementary Fig. 61). These results underscore the efficacy of employing a bilayer HSL at the bottom interface in mitigating trap-assisted non-radiative recombination and enhancing charge transport within the device. This improvement is attributed to the passivation of defects and robust interactions with the underlying interface of the perovskite layer^{35,36}.

These results were further verified by measuring the device's electroluminescence EQE measurement (EQEEL, Fig. 4d and Supplementary Fig. 62). The device utilizing Bz-PhpPACz (2.8 mM) demonstrated outstanding EQEEL, accompanied by a pronounced increase in EL emission intensity. This enhancement is indicative of a more efficient carrier injection process³⁷. Indeed, the EQEEL values for devices incorporating Bz-PhpPACz (2.8 mM) and Bz-PhpPACz (r) were determined to be 3.84% and 1.47%, respectively (Supplementary Fig. 62). In corroboration with the EQEEL findings, the quasi-Fermi level splitting (QFLS) was calculated using the photoluminescence quantum yield (PLQY) for both semi-stacked and fully-stacked devices. The analysis uncovered a significantly higher quantum yield and an augmented QFLS for the Bz-PhpPACz (2.8 mM) based devices, thereby reinforcing the previously discussed outcomes.

To further quantify the interfacial carrier extraction velocity of SAM molecules, transient reflection (TR) spectroscopy analysis was conducted on perovskite films deposited on FTO/SAM substrates. As shown in Fig. 4e and Supplementary Figs. 63–65, the Bz-PhpPACz (2.8 mM) sample exhibited the best carrier extraction ability with an S value of $3770 \pm 220 \text{ cm s}^{-1}$, while the Bz-PhpPACz (r) sample only had an S of $2500 \pm 270 \text{ cm s}^{-1}$. This indicated that the bilayer structure enhanced the ability to extract carriers through the Bz-PhpPACz SAM molecules. The faster extraction of carriers essentially increases the transient carrier density and the QFLS, i.e., increase V_{OC} and follows the trend of surface extraction velocity (Fig. 4f)^{34,38}. These results were also consistent with the theoretical calculations of electron localization function and charge density differences (Supplementary Figs. 66–68).

For evaluating devices stability, the unencapsulated devices were first tested under AM 1.5 G simulated solar irradiation at 25 °C and 80% relative humidity, which showed that the IPSC based on the bilayer structure had better stability. Specifically, the PCE of Bz-PhpPACz (2.8 mM) increased from an initial value of 25.11% to 25.35% after 400 s, while the PCE of Bz-PhpPACz (r) decreased from 23.82% to 23.34% (Supplementary Fig. 69). In adherence to the ISOS-L-II standard protocol, the degradation in performance of the unencapsulated IPSCs was monitored at the maximum power point (MPP) under persistent illumination within a nitrogen-filled environment at a temperature of $65 \pm 10 \text{ }^\circ\text{C}$ ³⁹. Following an extended period of over 3000 h of uninterrupted exposure, the IPSC utilizing Bz-PhpPACz (2.8 mM) demonstrated remarkable retention, maintaining 91.94% of its initial PCE, whereas the performance of the IPSC based on Bz-PhpPACz (r) variant decreased significantly to 30.72% (Fig. 4g). Additionally, to evaluate the thermal stability of the encapsulated devices, further assessments were carried out at a higher temperature of 85 °C under ambient conditions (RH $80 \pm 15\%$). These tests confirmed the stability of the bilayer SAM structure (Supplementary Fig. 70).

Finally, the improved wettability of Bz-PhpPACz (2.8 mM) bilayer HSL with perovskite also enables the fabrication of large-area IPSCs with 1 cm² active area, achieving a reverse scan PCE of 25.44% (Fig. 4h). The official certification (Supplementary Fig. 71) confirmed a PCE of 25.21% for the device, which featured an active area of 99.12 mm². This validation was provided by the Test and Calibration Center of New

Energy Device and Module at the Shanghai Institute of Microsystem and Information Technology, Chinese Academy of Sciences (SIMIT). The perovskite solar module using Bz-PhpPACz (2.8 mM) as the HSL achieved a PCE of 22.33%, with an aperture area of 19.80 cm², while a thicker HSL (4.2 mM) resulted in lower efficiency of 20.68% (Fig. 4i and Supplementary Fig. 72). Additionally, this study could be further extended to different perovskite compositions, incorporating the bilayer Bz-PhpPACz SAM into wide-bandgap perovskites such as Cs_{0.05}FA_{0.8}MA_{0.15}Pb(I_{0.755}Br_{0.255})₃ with a bandgap of 1.68 eV, achieving PCE of 22.46% and V_{OC} of 1.270 V (Supplementary Fig. 73). For Cs_{0.2}FA_{0.8}PbI_{1.8}Br_{1.2} with a bandgap of 1.78 eV, the PCE was 20.37% and the V_{OC} was 1.33 V (Supplementary Fig. 74). These findings highlighted the potential of bilayer SAM in future application of perovskite-based tandem solar cells.

Discussion

In this study, we designed and synthesized a SAM named Bz-PhpPACz, which was used as HSLs in the fabrication of IPSCs. The expanded π -conjugated system of Bz-PhpPACz enhanced intermolecular π - π interactions, facilitating the formation of an ordered bilayer structure with a hydrophilic surface. This structure is advantageous for high-quality large-area perovskite fabrication and better hole extraction. Remarkably, bilayer Bz-PhpPACz demonstrated high PCE and long-term stability and was highly versatile for different bandgap perovskites. These findings provide a promising pathway for the future of perovskite solar cells and emphasize the importance of continued research in this field.

Methods

Materials

The chemical reagents and solvents used for synthesis are all of reagent grade. 7H-dibenzo[*c,g*]carbazole, 1-bromo-4-iodobenzene, copper(I) iodide, potassium phosphate, palladium(II) acetate, 1,1'-bis(diphenylphosphino)ferrocene (dppf), and potassium acetate were purchased from Bide Pharmatech LTD. Diethyl phosphite, triethylamine, and were purchased from Energy Chemical Co. Ltd. Cyclohexane-1,2-diamine was purchased from Tokyo Chemical Industry. Bromotrimethylsilane (TMSBr) was purchased from J&K Scientific. Solvents and deuterium reagents were purchased from Adamas-beta Ltd. All materials are used without further purification unless otherwise noted.

For the materials used for perovskite solar cells fabrication included: formamidinium iodide (FAI; 99.99%, Advanced Election Technology CO.,Ltd), methylammonium iodide (MAI, 99.99%, Advanced Election Technology CO.,Ltd), methylammonium chloride (MACl, 99.99%, Greatcell Solar Materials Pty. Ltd.), methylammonium bromide (MABr, 99.99%, Greatcell Solar Materials Pty. Ltd.), lead iodide (PbI₂; 99.99%, TCI), lead(II) bromide (PbBr₂; 99.999%, Xi'an Polymer Light Technology Corp.), cesium iodide (CsI; 99.999%, Alfa Aesar), C60 (99.99%, Xi'an Polymer Light Technology Corp.), bathocuproine (BCP, 99.99%, Xi'an Polymer Light Technology Corp.), Piperazine dihydride (PDI, 99.99%, Xi'an Polymer Light Technology Corp.), molybdenum trioxide (MoO₃, 99.9995%, Alfa Aesar), water (H₂O; Alfa Aesar), N,N-dimethylformamide (DMF; 99.8%, J&K Scientific), 2-methoxyethanol (99.5%; J&K Scientific), dimethyl sulfoxide (DMSO; 99.9%, J&K Scientific), ethanol (99.5%; Sigma-Aldrich), isopropanol (IPA; 99.5%; Sigma-Aldrich), ethyl acetate (EA, 99.5%; Sigma-Aldrich), chlorobenzene (CB; 99.8%; Sigma-Aldrich), acetone (99.8%; Merck).

General characterizations of materials and thin film

¹H NMR, ¹³C NMR and ³¹P NMR spectra were characterized by Bruker AVANCE NEO 400 and Bruker AVANCE NEO 600. The UV-vis spectra were recorded using a PerkinElmer Lambda750S spectrophotometer. High-resolution electrospray ionization (HR-ESI) mass spectra were

obtained from Thermo Scientific Q Exactive mass spectrometer, operated in heated electrospray ionization (HESI) mode, and coupled with Thermo Scientific Ultimate 3000 system. The differential scanning calorimetry (DSC) and thermogravimetric analysis (TGA) measurements were performed on SDT Q600 instrument at a heating rate of 10 K min^{-1} in the range of $25\text{ }^{\circ}\text{C}$ to $800\text{ }^{\circ}\text{C}$ under a nitrogen atmosphere. Cyclic voltammetry (CV) was performed on Electrochemical Analyzer CHI760E (Chenhua Co. Ltd, Shanghai, China) using a three-compartment electrochemical cell, with samples in DMF containing $0.1\text{ M} [\text{Bu}_4\text{N}]\text{PF}_6$ as electrolyte and the ferrocenium/ferrocene (Fc^+/Fc) as internal standard under scan rate of 0.1 V s^{-1} . Ag/AgCl , glassy carbon, and platinum wire were used as the reference electrode, working electrode, and counter electrode, respectively.

The morphologies of the prepared samples were analyzed via SEM (Zeiss Merlin). A dual-beam focused ion beam (FIB, Helios 600i, FEI) combined with SEM was used to prepare transmission electron microscope (TEM) samples of the perovskite solar cells. The cross-sections of the perovskite solar cells were then observed using TEM (JEM-2100Plus, JEOL). The contact angle measurements were performed using a drop shape analyzer (DSA 25S, Kruss).

UPS and XPS measurements were performed using an ultrahigh vacuum surface analysis system equipped with an ULVAC-PHI 5000 VersaProbe III spectrometer. Ultraviolet photo-electron spectroscopy (UPS) was performed with He I (21.22 eV) acting as the excitation source at an energy resolution of 50 meV . XPS used monochromatic Al K_{α} radiation (1486.6 eV). All experiments were calibrated with respect to the Fermi edge of an atomically clean gold surface. The SAM samples used for XPS N 1s , P 2p , and Sn 3d spectra measurements were fabricated by spin-coating SAM solutions on FTO at varying concentrations. Subsequently, the samples were washed with a perovskite precursor solvent (DMF/DMSO (4:1, v/v)).

GIXRD measurements of the perovskite were performed on a Smartlab 9 kW diffractometer with a Göbel mirror attachment. The irradiation by the parallel $\text{CuK}_{\alpha 1,2}$ X-ray beams was fixed at a grazing angle of incidence (θ) of $0.1\text{--}1.0^{\circ}$. The detector was moved independently to collect diffraction data within the 2θ range ($5^{\circ}\text{--}60^{\circ}$) with a step size of 0.03° (2θ) at a fixed speed of 0.5 s/step .

The XRR measurements of the SAMs were conducted using a Smartlab 9 kW diffractometer to determine the SAM thin film thickness²⁸. X-ray was incident on the SAM's surface at a grazing angle of 0.05° , and data were collected within the 2θ range of 0° to 1.5° with a step size of 0.01° (2θ). The Kiessig fringes in XRR arise from interference between reflections from the top and bottom of the thin film layer. The position of these fringes corresponds to the thickness of the film layer²⁹. For larger layer thicknesses, the fringes shift to smaller 2θ values. The thickness of the SAM film can be calculated according to reported literature¹⁹. All the samples used for XRR measurement were washed by perovskite precursor solvent ((DMF/DMSO (4:1, v/v)) on ITO.

GIWAXS measurements were performed at the Synchrotron and Printable Electronics lab at Shenzhen Polytechnic with SaxesFocus using a Cu X-ray source (8.05 keV , 1.54 \AA) and a Pilatus3R 300 K detector. The incidence angle is 0.5° .

The photoluminescence (PL) measurement of the perovskite thin film (FTO/SAMs/perovskite) was conducted on the FLS1000 spectrometer (Edinburgh Instruments) with excitation using a 405 nm xenon lamp. The time-resolved PL (TRPL) and PLQY measurements for the perovskite films (FTO/SAMs/perovskite for TRPL and PLQY, FTO/SAMs/perovskite/C60 for PLQY) were performed on an FLS1000 spectrometer (Edinburgh Instruments) with excitation provided by a 475 nm pulsed laser. The samples were excited from the FTO side under ambient conditions. PL mapping was acquired using a laser scanning confocal Raman spectrometer (LabRAM HR Evolution) with excitation at 405 nm on the perovskite thin film.

Compositional depth profiling of perovskite films was conducted using a time-of-flight secondary-ion mass spectrometry (TOF-SIMS)

5 system (IONTOF). For depth profiling, a 500-eV Cs^+ sputter beam with a current of 28 nA was used to remove material layer-by-layer in an interlaced mode from a raster area of $300\text{ }\mu\text{m} \times 300\text{ }\mu\text{m}$. Mass spectrometry was performed on an area of $100\text{ }\mu\text{m} \times 100\text{ }\mu\text{m}$ in the center of the sputter crater.

Single crystal X-ray diffraction analysis

Single crystals of SAM molecules suitable for X-ray diffraction analysis were obtained by using vapor diffusion process at room temperature. PhpPACz and Bz-4PACz single crystals were obtained with hexane as antisolvent and THF as solvent. Bz-PhpPACz single crystal was obtained with ether as antisolvent and DMF as solvent, respectively.

A suitable crystal of PhpPACz , Bz-4PACz or Bz-PhpPACz was selected and mounted on a Bruker D8 VENTURE diffractometer equipped with a MetalJet D2 X-ray source and a Photon III detector. Data were measured using monochromatic $\text{Ga-K}\alpha$ radiation at $T = 100\text{ K}$ or 200 K . Data reduction, scaling and absorption corrections were performed using SAINT (Bruker, V8.38 A, 2013). The structure was solved with the ShelXT structure solution program using the Intrinsic Phasing solution method and by using Olex2 as the graphical interface. The model was refined with version 2016/6 of ShelXL (Sheldrick, 2015) using Least Squares minimization. All the CIF and structure factors are validated by the checkcif test and no alert A or B is reported. Crystallographic data reported in this paper were deposited in the Cambridge Crystallographic Data Centre (CCDC) (CCDC No. 2362431 for Bz-4PACz , CCDC No. 2361091 for PhpPACz , and CCDC No. 2361092 for Bz-PhpPACz , respectively (Supplementary Data1–3).

Polarization resolved infrared reflection spectroscopy

This experiment was done with a Thermo-Fisher Nicolet iS50 FT-IR spectrometer with a ZnSe waveplate with adjustable polarization direction. The samples were fixed on a holder and all spectra were obtained with a grazing angle reflectance method.

Transient reflection spectroscopy

The fundamental beam (800 nm , pulse duration $\sim 60\text{ fs}$, $\sim 5\text{ mJ pulse}^{-1}$, 1 kHz repetition rate, Coherent Astrella) is split in two beams. One beam was sent to an optical parametric amplifier (TOPAS, Light conversion) to generate the pump pulse (500 nm , 600 nm and 700 nm). The pump was chopped at a frequency of 500 Hz and its intensity was attenuated by two neutral density filter wheels. The other 800 nm beam was focused into a sapphire crystal to generate white light probe ($450\text{--}810\text{ nm}$) and detected with a CMOS detector (Timetech, TA-100). The probe pulses were delayed in time with respect to the pump pulses using a motorized translation stage mounted with a retroreflecting mirror. Probe delay can be up to $\sim 5\text{ ns}$, tuned by a delay line. The pump and probe were focused and overlapped on the surface of the sample spatially. For TR measurement, the incident angle for pump was around 0° and probe was around 45° .

Internal electron-hole quasi-Fermi level splitting

To quantify interface non-radiative recombination losses, we calculated the internal electron-hole QFLS from PLQY results by using the Eq. (1)⁴⁰:

$$\text{QFLS} = k_{\text{B}} \times \ln \left(\text{PLQY} \times \frac{J_{\text{G}}}{J_{0,\text{rad}}} \right) \quad (1)$$

Where k_{B} is Boltzmann constant. J_{G} is the generated current density at 1 sun, it is approximated with the short-circuit current density of the complete solar cell. $J_{0,\text{rad}}$ is the radiative recombination current in the dark, it is estimated by integrating the overlap of the photovoltaic external quantum efficiency of the full device (EQE_{PV}) with the black body radiative spectrum at 300 K over the energy. According to the

detailed balance theory:

$$q \int EQE_{PV}(E)\phi_{BB}(E)dE = J_{0,rad} \quad (2)$$

$$\phi_{BB} = \frac{1}{4\pi^2 h^3 c^2} \frac{E^2}{\exp\left(\frac{E}{k_B T}\right) - 1} \quad (3)$$

Where q , ϕ_{BB} , E , h , c , T represents elementary charge, black-body radiative spectrum, photon energy, Planck constant, speed of light in vacuum, and temperature. Assuming that the perovskite solar cell is at 300 K in thermal equilibrium with its environment. The value of $J_{0,rad}$ is 6.99×10^{-22} mA cm⁻² and 7.02×10^{-22} mA cm⁻² for Bz-PhpPACz (r) and Bz-PhpPACz (2.8 mM) based devices, respectively.

Preparation of perovskite precursor solutions for devices

For 1.53 eV bandgap perovskite, the perovskite precursor solution comprised 1 mL of 1.67 mM Cs_{0.03}FA_{0.97}PbI₃ and 16 μ L of 1 mM MAPbBr₃. For 1 mL of 1.67 mM Cs_{0.03}FA_{0.97}PbI₃, 13.02 mg CsI, 278.57 mg FAI, 840.72 mg PbI₂ (with 9.2% mol excess) and 18.10 mg MAI in 1 mL of DMF/DMSO (4:1, v/v). For 1 mL of 1 mM MAPbBr₃, 111.99 mg MABr and 400.77 mg PbBr₂ (with 9.2% mol excess) in 1 mL of DMF/DMSO (4:1, v/v). Please note, do not add any additives, as they may reduce the device performance.

For 1.68 eV bandgap perovskite, the perovskite precursor solution comprised 1.5 mM Cs_{0.05}FA_{0.8}MA_{0.15}Pb(I_{0.755}Br_{0.255})₃ (PbI₂ excess), specifically, 19.49 mg CsI, 206.36 mg FAI, 23.83 mg MABr, 489.24 mg PbI₂, 169.28 mg PbBr₂ in 1 mL of DMF/DMSO (4:1, v/v). Please note, do not add any additive, as it may reduce the device performance.

For 1.78 eV perovskite, the perovskite precursor solution comprised 1.4 mM Cs_{0.2}FA_{0.8}PbI_{1.8}Br_{1.2}, specifically, 72.75 mg CsI, 96.30 mg FAI, 69.98 mg FABr, 378.25 mg PbI₂, and 205.53 mg PbBr₂ in 1 mL of DMF/DMSO (3:1, v/v). Please note, do not add any additive, as it may reduce the device performance.

Fabrication of devices with 1.53 eV perovskite

Planar p-i-n IPSCs were fabricated using fluorine doped tin oxide (FTO), SAM, perovskite, C60, BCP, and copper (Cu) as the anode, HSL, light absorber layer, electron transport layer (ETL) and cathode, respectively. FTO (8 Ω) were washed with cleaning fluid, deionized water, isopropanol, acetone, ethanol, and sequentially. The FTO was then treated with UV-ozone for 20 min.

For devices using Bz-PhpPACz, and Bz-4PACz as the HSLs, SAMs solution with various concentrations (0.7 mM, 1.4 mM, 2.1 mM, 2.8 mM, 3.5 mM, and 4.2 mM) were dissolved in a methanol and 2-methoxyethanol solution (100: 2, v/v) and statically spun-coated onto FTO substrates at 3000 rpm for 30 s. The substrates were then annealed at 120 $^{\circ}$ C for 10 min. For example, the samples of Bz-PhpPACz fabricated with concentration of 2.8 mM were denoted as Bz-PhpPACz (2.8 mM). While the sample of Bz-PhpPACz (r) was fabricated by spin-coating Bz-PhpPACz solution with concentration of 2.8 mM with the same procedure and then rinsing by isopropanol thoroughly. After that, the substrates were then annealed at 120 $^{\circ}$ C for 10 min.

The perovskite film was deposited on the HSLs by a solvent engineering method. Spread perovskite solution over HSL and spin-coated in two steps, namely, 1000 rpm for 7 s and 5000 rpm for 30 s. Then, with 15 s of spin time remaining, chlorobenzene (150 μ L for FTO with area of 15 mm \times 15 mm and 190 μ L for FTO with area of 22 mm \times 20 mm) was slowly dispensed onto the middle of the substrate and the films were annealed at 100 $^{\circ}$ C for 0.5 h. For the passivation treatment, the IPA solution of PDI (0.01 mM) was spin-coated on the perovskite surface at 3000 rpm for 30 s, followed by annealing at 100 $^{\circ}$ C for 5 min. The surface was then rinsed with IPA at 5000 rpm and annealed again at 100 $^{\circ}$ C for 1 min. The thickness of the as-fabricated perovskite layer

was determined to be \sim 700 nm by cross-sectional SEM images. C60 (40 nm), BCP (8 nm) and a metallic copper (100 nm) electrode were thermally evaporated in a vacuum chamber at a pressure set at $<4 \times 10^{-6}$ Pa through a shadow mask. Finally, the anti-reflection film (Mitsubishi) is attached to the glass surface. For stability testing, the substrates with deposited C60 were transferred to an atomic layer deposition system (SUPERALD, LLC). At 90 $^{\circ}$ C, 20 nm of SnO₂ (99.9999% purity) was deposited to replace the previous BCP layer, the devices were then encapsulated.

Fabrication of devices with wide bandgap perovskite

The device structure is the same as described above. For the wide-bandgap perovskite devices, a SAM system consisting of Bz-PhpPACz was used as the HSL. SAMs solution with concentration of 2.8 mM was dissolved in a methanol and 2-methoxyethanol solution (100:2, v/v) and statically spun-coated onto FTO substrates at 3000 rpm for 30 s. The substrates were then annealed at 120 $^{\circ}$ C for 10 min. The perovskite film was deposited on the HSLs by a solvent engineering method. For 1.68 eV PSCs, perovskite films were spin-coated at 2000 rpm for 45 s with an acceleration of 400 rpm s⁻¹, then followed with 7000 rpm for 10 s with an acceleration of 5000 rpm s⁻¹. Chlorobenzene of 200 μ L was dropped in the center of the substrates 12 s before the end of the spin-coating process. For 1.78 eV PSCs, perovskite films were spin-coated at 1000 rpm for 5 s and 4000 rpm for 40 s. Then, with 8–9 s of spin time remaining, chlorobenzene (180 μ L for FTO with area of 15 mm \times 15 mm) was slowly dispensed onto the middle of the substrate and the films were annealed at 100 $^{\circ}$ C for 0.5 h. For the passivation treatment, the IPA solution of PDI (0.01 mM) and PEAI (0.01 mM) was spin-coated on the perovskite surface at 5000 rpm for 30 s, followed by annealing at 100 $^{\circ}$ C for 5 min. The surface was then rinsed with IPA at 5000 rpm and annealed again at 100 $^{\circ}$ C for 5 min. C60 (40 nm), BCP (8 nm) and a metallic copper (100 nm) electrode were thermally evaporated in a vacuum chamber at a pressure set at $<4 \times 10^{-6}$ Pa through a shadow mask. Finally, the anti-reflection film (Mitsubishi) is attached to the glass surface.

Fabrication of module

Perovskite solar modules (6.5 \times 6.5 cm², Supplementary Fig. 72) were fabricated using a spin-coating process. A 355 nm laser beam with a power of 3 W was used for laser patterning the P1, P2, P3, and P4 line. Before cleaning the FTO glass, the FTO layer was removed from the substrate using the P1 laser at a speed of 500 mm s⁻¹, a frequency of 30 kHz, and a pulse width of 8 μ s. After ETL deposition, a laser with a cutting speed of 500 mm s⁻¹, a frequency of 30 kHz, and a pulse width of 2 μ s was used to remove all deposited layers (P2). Low-energy laser ablation was applied two or more times to remove the functional layers, minimizing damage to the FTO. After copper deposition, the P3 laser was used to remove all deposited layers by scanning at a speed of 500 mm s⁻¹, a frequency of 30 kHz, and a pulse width of 3 μ s. Low-energy laser ablation was applied again in P3 to further minimize damage to the FTO. For P4, a laser with a scanning speed of 500 mm s⁻¹, a frequency of 30 kHz, and a pulse width of 5 μ s was utilized to eliminate all deposited materials. The line widths of P1, P2, and P3 were approximately 60 μ m, 120 μ m, and 120 μ m, respectively. The distance between P1 and P2, as well as P2 and P3, was around 50 μ m.

Device characterization

A Keithley 2400 SourceMeter measurement unit was used along with an Oriol xenon lamp (450 W) with an AM 1.5 filter to characterize the solar cells in air under AM 1.5 G illumination at 100 mW cm⁻² (Newport Oriol 1 kW solar simulator) after calibration with a KG5 filter certified by the National Renewable Energy Laboratory. The current density-voltage (J - V) curves for all devices (active area: 0.0715 cm² and 1 cm²) were measured at a scanning speed of 0.01 V per step with dwell time of 100 ms under forward and reverse direction. The stabilized power

output was measured at the maximum power point (MPP) voltage. The incident-photon-to-current-efficiency (IPCE) spectra were recorded using a constant 100 W xenon lamp source with an automated monochromatic filter and a rectangular spot size of 0.76 mm × 1.0 mm. The IPCE measurements were conducted within the wavelength range from 300 to 900 nm using a chopping frequency of 4 Hz (IQE-200B model). The light intensity dependences of the short circuit current density (J_{SC}) and open circuit voltage (V_{OC}) characteristics were measured using a 10–97.5% light reduction film to adjust the light intensity of the solar simulator in air under AM 1.5 G illumination.

Electrical impedance spectroscopy (EIS) measurements were conducted using an electrochemical workstation (IM6ex, Zahner) with a frequency range from 10 Hz to 4 MHz under an applied voltage of 0.9 V in the dark. For the Mott-Schottky measurements, the capacitance-voltage measurements were conducted at a fixed frequency (10 kHz) using an IM6ex (Zahner) instrument. The Mott-Schottky plot was obtained in the dark, ranging from 0 V to 1.2 V in the positive direction, with an active area of 0.1 cm².

For the trap density of states (TDOS) Method, the C – V measurement, the DC bias was from –2 V to 2 V for the samples. The scanning range of the AC frequency was from 10 Hz to 10 MHz. The TDOS ($N_T(E_\omega)$) was described as:

$$N_T(E_\omega) = -\omega(dC/d\omega)(V_{bi}/qkTW) \quad (4)$$

where W is the depletion width and V_{bi} is the built-in potential of devices, derived from the Mott-Schottky analysis of the C – V measurement, T , k , q , ω , and C are temperature angular, Boltzmann's constant, elementary charge, frequency, and specific capacitance, respectively.

The demarcation energy is:

$$E\omega = kT \ln(\omega_0/\omega) \quad (5)$$

where ω_0 is the attempt-to-escape angular frequency ($2 \times 10^{11} \text{ s}^{-1}$)⁴¹.

Hole-only devices (FTO/SAMs/perovskite/MoO₃/Au) were fabricated according to the IPSC fabrication procedure. MoO₃ (8 nm) and Au (80 nm) were thermally evaporated in a vacuum chamber at a pressure set below 4×10^{-6} Pa. The dark J – V characteristics of the hole-only devices were measured using a Keithley 2400 SourceMeter. For electroluminescence testing, a Keithley 2400 SourceMeter was employed in conjunction with the XPQY-EQE-200-1100 (Xi Pu Optoelectronics Technology Co., Ltd.) connected to an integrating sphere.

Operational stability tests were performed at the MPP for the unencapsulated devices under AM 1.5 G illumination (100 mW cm^{–2}) at 65 ± 10 °C in a N₂ atmosphere within a light-emitting diode (LED)-based solar simulator. The bias at the MPP was calculated and then applied automatically. For thermal stability tests, the MPP for the encapsulated devices under AM 1.5 G illumination (100 mW cm^{–2}) at 85 °C air atmosphere (RH 80 ± 15%) within a LED-based solar simulator.

Computational method

The static DFT calculations were performed using the Vienna Ab Initio Simulation Package (VASP), while the ab initio molecular dynamics (AIMD) simulations were conducted with the CP2K package. All calculations employed periodic boundary conditions. The projector augmented wave (PAW) pseudopotential described the ion-core electron interaction, and the Perdew-Burke-Ernzerhof (PBE) functional with a plane-wave cutoff energy of 400 eV described the exchange-correlation energy of valence electrons. Grimme's D3 corrections were applied to account for dispersion interaction. The energy convergence criterion for structure optimization, including lattice parameters and internal atomic positions, was set to 10^{-6} eV for each self-consistent field (SCF) iteration, and the maximum force convergence criterion for geometry optimization was set to $0.02 \text{ eV } \text{Å}^{-1}$. Born-Oppenheimer AIMD simulations were performed with an integration time step of

0.5 fs, maintaining the system at 300 K using the Bussi et al. thermostat in a canonical isothermal–isochoric (NVT) ensemble. All AIMD simulations were performed at the Γ point.

The FTO model was constructed using bulk SnO₂, with the (001) surface selected as the substrate. A 3×3 supercell of the tetragonal SnO₂ (001) surface was organized with a slab consisting of three O–Sn–O layers, while the bottom layer was kept frozen. Our simulation introduced one oxygen vacancy (O_V) on the FTO surface, following previous literature. A vacuum of 20.0 Å was inserted along the [001] direction to avoid unphysical interactions between the slabs. The FTO model, sized at $14.50 \times 14.50 \times 30.11 \text{ Å}^3$, was used to study the molecular dynamic behavior of a single SAM molecule on the FTO surface. Gamma point k-point sampling was employed for Brillouin-zone integration. To investigate the packing model of multiple SAM molecules on the FTO surface, a larger FTO model size of $28.99 \times 28.99 \times 45.00 \text{ Å}^3$ was used. The systems were equilibrated for 2 ps in the NVT ensemble, followed by an 8 ps production run. AIMD simulations started from DFT-optimized structure to investigate the dynamic behavior of SAM molecules. The system was equilibrated for approximately 10 ps to achieve the most stable configuration on FTO surface.

The size of the upper three-layer FAPbI₃ perovskite model is $19.47 \times 26.01 \times 42.26 \text{ Å}^3$. Binding energies were calculated as:

$$\Delta E_{\text{ads}} = E_{\text{tot}} - E_{\text{pvk}} - E_{\text{mol}} \quad (6)$$

where E_{tot} is the energy of the final relaxed configuration (molecule on perovskite surface); E_{pvk} is the energy of the final configuration of the perovskite bulk; and E_{mol} is the energy of the final configuration of the isolated SAM molecule.

The charge difference between the SAM molecules and the perovskite is represented as:

$$\Delta\rho = \rho_{\text{SAM/perovskite}} - \rho_{\text{SAM}} - \rho_{\text{Perovskite}} \quad (7)$$

The intermolecular interaction energies were calculated as:

$$\Delta E_i = E_{\text{tot}} - 2 * E_{\text{mol}} \quad (8)$$

where E_{tot} is the energy of the two molecules in same system; and E_{mol} is the energy of a single isolated molecule.

Reporting summary

Further information on research design is available in the Nature Portfolio Reporting Summary linked to this article.

Data availability

All data generated or analyzed during this study are included in the published article and its Supplementary Information. Additional data are available from the corresponding author on request.

References

- An, Y. et al. Optimizing crystallization in wide-bandgap mixed halide perovskites for high-efficiency solar cells. *Adv. Mater.* **36**, 2306568 (2024).
- Liu, J. et al. Efficient and stable perovskite-silicon tandem solar cells through contact displacement by MgFx. *Science* **377**, 302–306 (2022).
- He, R. et al. Improving interface quality for 1-cm² all-perovskite tandem solar cells. *Nature* **618**, 80–86 (2023).
- Zhou, S. et al. Aspartate all-in-one doping strategy enables efficient all-perovskite tandems. *Nature* **624**, 69–73 (2023).
- Wu, T. et al. Self-Assembled Monolayer Hole-Selective Contact for Up-Scalable and Cost-Effective Inverted Perovskite Solar Cells. *Adv. Funct. Mater.* **34**, 2316500 (2024).

6. Li, M. et al. Self-assembled monolayers for interfacial engineering in solution-processed thin-film electronic devices: design, fabrication, and applications. *Chem. Rev.* **124**, 2138–2204 (2024).
7. Chen, H. et al. Improved charge extraction in inverted perovskite solar cells with dual-site-binding ligands. *Science* **384**, 189–193 (2024).
8. Liu, S. et al. Buried interface molecular hybrid for inverted perovskite solar cells. *Nature* **632**, 536–542 (2024).
9. Deng, X. et al. Co-assembled monolayers as hole-selective contact for high-performance inverted Perovskite Solar cells with optimized recombination loss and long-term stability. *Angew. Chem. Int. Ed.* **61**, e202203088 (2022).
10. Park, S. M. et al. Low-loss contacts on textured substrates for inverted perovskite solar cells. *Nature* **624**, 289–294 (2023).
11. Peng, W. et al. Reducing nonradiative recombination in perovskite solar cells with a porous insulator contact. *Science* **379**, 683–690 (2023).
12. Li, J. et al. Enhancing the efficiency and longevity of inverted perovskite solar cells with antimony-doped tin oxides. *Nat. Energy* **9**, 308–315 (2024).
13. Zhang, S. et al. Minimizing buried interfacial defects for efficient inverted perovskite solar cells. *Science* **380**, 404–409 (2023).
14. Liang, Z. et al. Homogenizing out-of-plane cation composition in perovskite solar cells. *Nature* **624**, 557–563 (2023).
15. Li, W. et al. Self-assembled molecules as selective contacts for efficient and stable perovskite solar cells. *Mater. Chem. Front.* **8**, 681–699 (2024).
16. Li, E. et al. Bonding strength regulates anchoring-based self-assembly monolayers for efficient and stable perovskite solar cells. *Adv. Funct. Mater.* **31**, 2103847 (2021).
17. Zhang, S. et al. Conjugated self-assembled monolayer as stable hole-selective contact for inverted perovskite solar cells. *ACS Mater. Lett.* **4**, 1976–1983 (2022).
18. Li, C. et al. Fully aromatic self-assembled hole-selective layer toward efficient inverted wide-bandgap perovskite solar cells with ultraviolet resistance. *Angew. Chem. Int. Ed.* **63**, e202315281 (2024).
19. Qu, G. et al. Conjugated linker-boosted self-assembled monolayer molecule for inverted perovskite solar cells. *Joule* **8**, 2123–2134 (2024).
20. Puerto Galvis, C. E. et al. Challenges in the design and synthesis of self-assembling molecules as selective contacts in perovskite solar cells. *Chem. Sci.* **15**, 1534–1556 (2024).
21. Magomedov, A. et al. Self-assembled hole transporting monolayer for highly efficient perovskite solar cells. *Adv. Energy Mater.* **8**, 1801892 (2018).
22. Al-Ashouri, A. et al. Conformal monolayer contacts with lossless interfaces for perovskite single junction and monolithic tandem solar cells. *Energy Environ. Sci.* **12**, 3356–3369 (2019).
23. Aktas, E. et al. Understanding the perovskite/self-assembled selective contact interface for ultra-stable and highly efficient p-i-n perovskite solar cells. *Energy Environ. Sci.* **14**, 3976–3985 (2021).
24. Jiang, W. et al. π -Expanded Carbazoles as hole-selective self-assembled monolayers for high-performance perovskite solar cells. *Angew. Chem. Int. Ed.* **61**, e202213560 (2022).
25. Sun, A. et al. High Open-Circuit Voltage (1.197 V) in Large-Area (1 cm²) inverted perovskite solar cell via interface planarization and highly polar self-assembled monolayer. *Adv. Energy Mater.* **14**, 2303941 (2024).
26. Jiang, W. et al. Spin-coated and vacuum-processed hole-extracting self-assembled multilayers with H-aggregation for high-performance inverted perovskite solar cells. *Angew. Chem. Int. Ed.* **63**, e202411730 (2024).
27. Ohki, S. & Aono, O. Phospholipid bilayer-micelle transformation. *J. Colloid Interface Sci.* **32**, 270–281 (1970).
28. Lange, I. et al. Tuning the work function of polar zinc oxide surfaces using modified phosphonic acid self-assembled monolayers. *Adv. Funct. Mater.* **24**, 7014–7024 (2014).
29. Tidswell, I. M. et al. X-ray specular reflection studies of silicon coated by organic monolayers (alkylsiloxanes). *Phys. Rev. B* **41**, 1111–1128 (1990).
30. Liao, Q. et al. Self-assembled donor-acceptor hole contacts for inverted perovskite solar cells with an efficiency approaching 22%: The impact of anchoring groups. *J. Energy Chem.* **68**, 87–95 (2022).
31. Wadayama, T. et al. Carbon monoxide adsorption on Co deposited Pt (100)-hex: IRRAS and LEED investigations. *Appl. Surf. Sci.* **256**, 4517–4521 (2010).
32. Kimmel, G. A. et al. Polarization- and Azimuth-Resolved infrared spectroscopy of water on TiO₂ (110): anisotropy and the hydrogen-bonding network. *J. Phys. Chem. Lett.* **3**, 778–784 (2012).
33. Xue, J. et al. Reconfiguring the band-edge states of photovoltaic perovskites by conjugated organic cations. *Science* **371**, 636–640 (2021).
34. Qu, G. et al. Dopant-Free Phthalocyanine hole conductor with thermal-induced holistic passivation for stable perovskite solar cells with 23% efficiency. *Adv. Funct. Mater.* **32**, 2206585 (2022).
35. Cao, Q. et al. Efficient and stable inverted perovskite solar cells with very high fill factors via incorporation of star-shaped polymer. *Sci. Adv.* **7**, eabg0633 (2021).
36. Li, X. et al. Modulating the deep-level defects and charge extraction for efficient perovskite solar cells with high fill factor over 86. *Energy Environ. Sci.* **15**, 4813–4822 (2022).
37. Rai, M. et al. Effect of Perovskite thickness on electroluminescence and solar cell conversion efficiency. *J. Phys. Chem. Lett.* **11**, 8189–8194 (2020).
38. Gong, S. et al. A hot carrier perovskite solar cell with efficiency exceeding 27% enabled by ultrafast hot hole transfer with phthalocyanine derivatives. *Energy Environ. Sci.* **17**, 5080–5092 (2024).
39. Khenkin, M. V. et al. Consensus statement for stability assessment and reporting for perovskite photovoltaics based on ISOS procedures. *Nat. Energy* **5**, 35–49 (2020).
40. Caprioglio, P. et al. On the relation between the open-circuit voltage and Quasi-Fermi level splitting in efficient Perovskite solar cells. *Adv. Energy Mater.* **9**, 1901631 (2019).
41. Samiee, M. et al. Defect density and dielectric constant in perovskite solar cells. *Appl. Phys. Lett.* **105**, 153502 (2014).

Acknowledgements

This work was supported by the National Key Research and Development Project of the Ministry of Science and Technology of China (no. 2021YFB3800103), the Shenzhen Science and Technology Innovation Commission (20231115141039001, JCYJ20220530112801004), the Major Program of Guangdong Basic and Applied Research (Grant No. 2019B030302009). S.C. acknowledge the funding support by the Natural Science Foundation of Guangdong Province under contract number 2023A1515011145, Guangdong Major Project of Basic and Applied Basic Research (2023B0303000002), Guangdong Provincial University Science and Technology Program (grant no. 2023KTSCX119) and Shenzhen Science and Technology Innovation Commission under contract numbers JCYJ20220530114809022 and ZDSYS20220527171403009.

Author contributions

Z.-X.X., G.Q., and S.C. conceived and designed the research. G.Q. and Y.D. carried out the fabrication and major characterization of IPSCs. L.Z. synthesized and characterized the SAM molecules. Y.Q. conducted theoretical simulations. G.Q. and Y.T. carried out the fabrication and major characterization of WBG IPSCs, large area devices and mini-module. S.G. and X.C. performed ultrafast spectroscopic and IR measurements. X.-Y.C. performed the single crystal analysis. P.X., J.F., C.G., and G.L. performed PL mapping, SEM, FIB, and TEM measurements. H.X. conducted the

electroluminescence testing. F.W. and H.H. were responsible for the GIWAXS testing. J.Y. and S.C. conducted the stability testing. C.Q. contributed for drawing the schematic diagrams. X.C. and A.J. contributed to the analysis and provided advice. G.Q., L.Z., Y.Q., and Z-X.X. wrote the initial draft and all authors contributed to the final paper.

Competing interests

The authors declare no competing interests.

Additional information

Supplementary information The online version contains supplementary material available at <https://doi.org/10.1038/s41467-024-55523-0>.

Correspondence and requests for materials should be addressed to Alex K.-Y. Jen, Xihan Chen or Zong-Xiang Xu.

Peer review information *Nature Communications* thanks the anonymous reviewer(s) for their contribution to the peer review of this work. A peer review file is available.

Reprints and permissions information is available at <http://www.nature.com/reprints>

Publisher's note Springer Nature remains neutral with regard to jurisdictional claims in published maps and institutional affiliations.

Open Access This article is licensed under a Creative Commons Attribution-NonCommercial-NoDerivatives 4.0 International License, which permits any non-commercial use, sharing, distribution and reproduction in any medium or format, as long as you give appropriate credit to the original author(s) and the source, provide a link to the Creative Commons licence, and indicate if you modified the licensed material. You do not have permission under this licence to share adapted material derived from this article or parts of it. The images or other third party material in this article are included in the article's Creative Commons licence, unless indicated otherwise in a credit line to the material. If material is not included in the article's Creative Commons licence and your intended use is not permitted by statutory regulation or exceeds the permitted use, you will need to obtain permission directly from the copyright holder. To view a copy of this licence, visit <http://creativecommons.org/licenses/by-nc-nd/4.0/>.

© The Author(s) 2024